AIAA 98-0959

# STUDY OF THE GAS JET IN A CLOSE-COUPLED GAS-METAL ATOMIZER

P. I. Espina*
*National Institute of Standards and Technology*
*Gaithersburg, Maryland 20899*
and
U. Piomelli†
*University of Maryland*
*College Park, Maryland 20742*

## Abstract

The gas-only flow in a close-coupled, gas-metal atomizer is studied to determine the influence of operational parameters on the structure of the flow field. A methodology developed for the study of supersonic base flows is validated by comparing numerical results to atomization experimental findings. It is found that a 10% reduction in the production of turbulence dissipation in the Chien $k$-$\epsilon$ model leads to improved agreement with experiments.

A parametric study is conducted to determine the effects of jet exit pressure ratio, and gas heating on the structure of the flows. Comparisons between Schlieren images and numerical results are found to be in good qualitative agreement; the numerical method predicted the experimental values of base pressure, however, only within 10-20% of the experimental values. Results from the pressure ratio study led to a description of the observed base-pressure behavior on the basis of the resulting jet structure. The temperature ratio results indicated that the industrial practice of gas-heating may be detrimental to the atomization process due to a global reduction of the momentum of the gas flow field.

## Nomenclature

| | |
|---|---|
| $a$ | speed of sound |
| $C_{\epsilon 1}$ | production of turbulence dissipation proportionality constant |
| $C_{\epsilon 2}$ | dissipation of turbulence dissipation proportionality constant |
| $C_f$ | friction coefficient, $2\,\tau_w/\rho_r a_r^2$ |
| $CL$ | axis of symmetry |
| ccw | counter clockwise |
| $k$ | turbulence kinetic energy |
| $L$ | length or extension |
| $M$ | Mach Number |
| $P$ | pressure |
| $R$ | liquid-delivery-tube radius |
| $r$ | radius or radial coordinate |
| $s$ | coordinate direction parallel to the exterior surface of the liquid-delivery-tube |
| $S_{ij}$ | strain-rate tensor, $(\partial u_i/\partial x_j + \partial u_j/\partial x_i)/2$ |
| $T$ | temperature |
| $u$ | mean streamwise velocity |
| $x$ | axial coordinate |
| $\alpha$ | angle |
| $\epsilon$ | turbulence dissipation rate |
| $\gamma$ | specific heat ratio |
| $\rho$ | density |
| $\mathcal{P}_\epsilon$ | production term in the turbulence dissipation equation |
| $\tau_w$ | shear stress at the wall |

*Subscripts*

| | |
|---|---|
| *cold* | refers to property of jet at $T_e/T_r = 0.65$ |
| *dt* | liquid-delivery-tube |
| *e* | annular channel exit |
| *exp* | experimental value |
| *hot* | refers to property of jet at $T_e/T_r = 1.31$ |
| *jet* | annular channel |
| *max* | maximum value |
| *num* | numerical value |
| *o* | stagnation condition or outer radius |
| *r* | receiving chamber |

*Mechanical Engineer, Fluid Flow Group, Bldg. 230, Rm. 105. Member AIAA.

†Associate Professor, Department of Mechanical Engineering. Senior Member AIAA.

*Superscripts*

$*$ nondimensional unit (normalized by the receiving chamber property)

## Introduction

Gas-metal atomization is a process by which liquid metal is transformed into metal powder. The metal powders produced by gas-metal atomization exhibit chemical homogeneity and refined microstructures which cannot be obtained by conventional casting techniques. Given their enhanced properties, the products made from these powders find applications ranging from jet engine parts to medical implants.[1]

The heart of a gas-metal atomizer is a device called the *atomization die*. This device, which contains both gas and liquid-metal conduits, is used to force the interaction between a high speed gas jet and a liquid stream of molten metal. The interaction between these streams exchanges momentum, accelerating the liquid into instabilities and disruption. Typically, this disruption process continues until the droplets reach a Weber number small enough to preclude further disruption after which they solidify in flight. At the end of the process, the powder is separated from the gas and is consolidated into products in post-processing operations.

Atomization dies can be of two types: *free-fall*, or *close-coupled*.[2] In free-fall atomizers (Figure 1, left), the stream of molten metal is allowed to fall unrestricted until it interacts with the gas jet. In close-coupled atomizers (Figure 1, right), the stream of molten metal is delivered by a ceramic conduit (known as the liquid-delivery-tube) to the interaction zone with the gas jets. Close-coupled atomizers are more difficult to operate but they tend to produce finer powers than free-fall atomizers. Given that the benefits of metal powders generally improve with smaller particle sizes,[3] close-coupled atomizers are in high demand and their control is of significant interest to the metal-powder producing industry.

Because the control of a molten stream of metal at a temperature near 1700 K can be difficult, strategies to control the gas-delivery-system in atomizers require a physical understanding of the gas-only flow (see Figure 2). Thus, in this investigation, the gas-only flow in a close-coupled, gas-metal atomizer is studied to determine the influence of operational

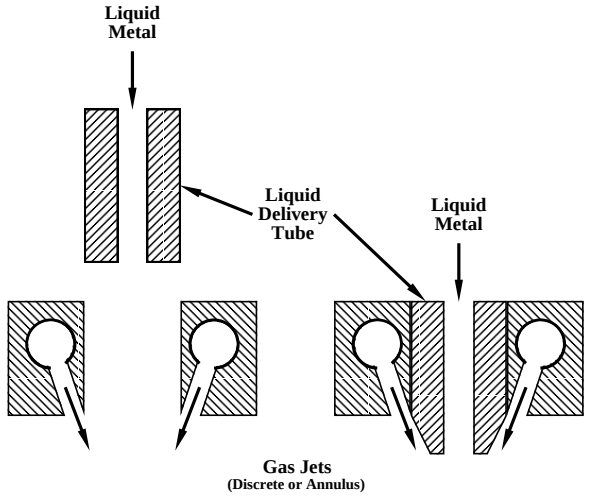


Figure 1. Schematic diagrams of gas-metal atomization dies: free-fall atomizer (left), close-coupled atomizer (right).

parameters on the structure of the flow field. This is not to say that the liquid metal will have no influence in the final structure of the metal spray, but knowledge acquired about the gas-only flow can lead to both design and control tools for future generations of gas-metal atomizers.

The study presented here considers the gas-only flow produced by a generic close-coupled gas-metal atomizer. By "generic," it is implied that the geometry of the atomization nozzle assembly was selected to be representative of numerous designs used by other researchers and industry.[4] The operational parameters are based on those typically used for the production of metal powder.[5] Figure 3 schematically shows the geometry considered, and Table 1 contains a summary of the operational parameters with their typical associated ranges.

Both experimental and numerical results are presented herein and the effects of process parameters on the formation of liquid-metal droplets are discussed. First, applying the methodology used to study similar base flows,[4,6] the atomizer jet at baseline conditions (see Table 1) is studied using both numerical and experimental techniques. Experimentally, the conventional jet flow is examined using Schlieren photography searching for the position of shock waves, expansion fans, separation lines, and shear layers. Using these data, comparisons are made with the numerical results, focusing on the location of the various flow features in the jet, thus enabling a critical evaluation of the turbulence model parameters.

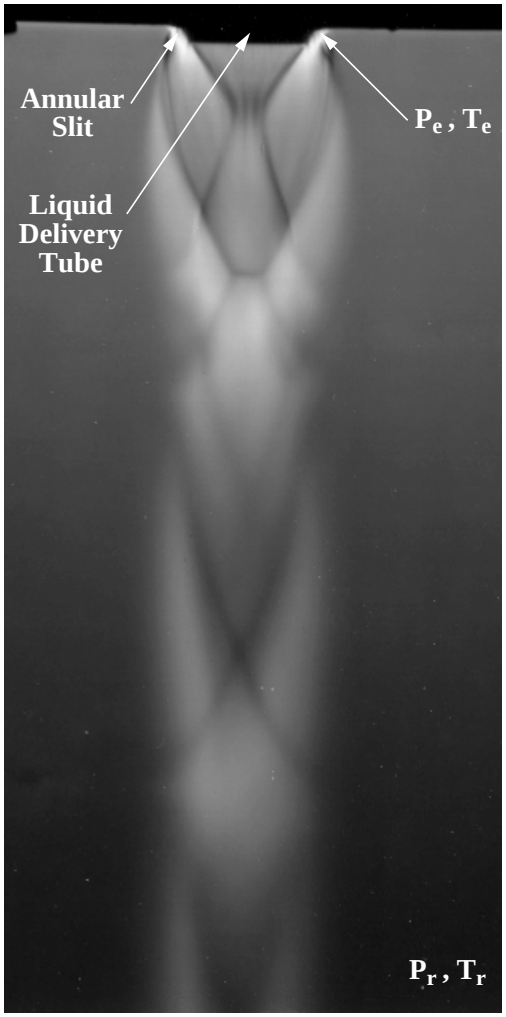


Figure 2. Schlieren image of the gas jet produced by a close-coupled gas-metal atomizer at baseline operating conditions.

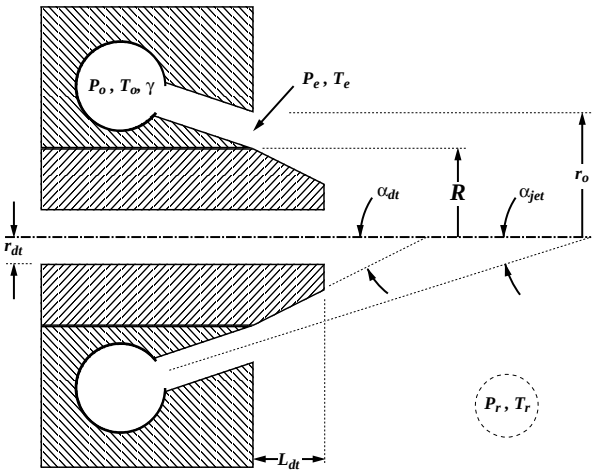


Figure 3. Schematic diagram of the annular jet, close-coupled atomization die studied in this investigation (geometry rotated 90° ccw from its normal operational orientation).

| *Parameter* | *Operational Range* | *Baseline* |
|---|---|---|
| $R$ | | $4.825\ mm$ |
| $r_o/R$ | | 1.0632 |
| $\alpha_{jet}$ | $0° \rightarrow 27.5°$ | 22.5° |
| $\alpha_{dt}$ | $0° \rightarrow 27.5°$ | 22.5° |
| $L_{dt}/R$ | $0 \rightarrow 0.6$ | 0.6 |
| $r_{dt}/R$ | $0.21 \rightarrow 0.31$ | 0.31 |
| gas species | Ar, He, or $N_2$ | Ar |
| $P_r$ | $0.5 \rightarrow 2.0\ atm$ | $1\ atm$ |
| $P_e/P_r$ | $3.8 \rightarrow 53.5$ | 33 |
| $T_r$ | $293 \rightarrow 600\ K$ | $293\ K$ |
| $T_e/T_r$ | $0.65 \rightarrow 1.31$ | 0.65 |

Table 1. Typical parameter ranges used during the operation of the generic gas-metal atomizer in Figure 3.[5]

Following this validation stage, a parametric study is conducted to determine the effects of various process parameters on the structure of the atomization jet. Among the parameters evaluated are: the dimensionless jet exit pressure, $P_e/P_r = 6.6 \rightarrow 46$, and the dimensionless jet exit temperature, $T_e/T_r = 0.65 \rightarrow 1.31$. Using the data obtained it is concluded that, with some experimental verification, parameterization studies such as this can be a very cost effective way to optimize gas-metal atomizers.

## Numerical Method

### Governing Equations

The axisymmetric, steady, compressible flow in a close-coupled, gas-metal atomizer is governed by the non-reacting Navier-Stokes equations. In this work, the Navier-Stokes equations are solved in strong, conservative form in a curvilinear coordinate system.[7] The fluid is assumed to be a thermally- and calorically-perfect gas that exhibits a Newtonian stress-strain behavior. The Prandtl number is assumed to be constant, while the molecular viscosity and the thermal conductivity are assumed to

be functions of the local static temperature. These assumptions render the dimensionless thermal conductivity and molecular viscosity equal in value, and thus, they are both computed using the Sutherland viscosity law.[8]

## Numerical Algorithm

The solution to the Navier-Stokes equations was accomplished using the NPARC code,[9] which is a descendant of the NASA ARC code.[7] In this implementation of the Beam-Warming approximate factorization algorithm,[10] time advancement is performed using a backward Euler scheme. Approximate factorization is used to facilitate solution of the resulting system of equations, and both second- and fourth-order artificial dissipation are introduced to suppress dispersion errors near shock waves and decoupling of even-odd modes due to the second-order central difference discretization. The resulting equations yield a series of block pentadiagonal systems that can be linearized by time-advancing the viscous fluxes and the axisymmetric source terms explicitly. This results in a series of scalar pentadiagonal systems that are solved directly using the Thomas algorithm.

## Turbulence Model

Solutions to the atomization gas-only flows were obtained using a compressible implementation[11] of Chien's $k$-$\epsilon$ turbulence model.[12] However, in this investigation, the value of the $C_{\epsilon 1}$ constant in Chien's model was altered to correct for an overprediction in the production of turbulence kinetic energy dissipation observed during the simulation of supersonic base flows.[6] Further details on this modification are provided in the results section.

In the NPARC code, the solution of the turbulence equations is time-lagged with respect to the solution of the flow equations and was accomplished using the algorithm suggested by Sahu and Danberg.[13] In this algorithm, second-order, upwind differences are used to approximate the spatial derivatives, and approximate factorization is used to facilitate solution of the resulting equation. This renders the use of artificial dissipation unnecessary, given the inherent smoothing properties of the upwind differences. The resulting equation yields a series of block tridiagonal systems that are solved directly using a block version of the Thomas algorithm.

## Physical Domain and Boundary Conditions

The computational domain used in this investigation (see Figure 4) follows the specifications of the close-coupled atomizer used by Ridder and Biancaniello.[5] However, it changes their discrete jet geometry to an annular jet version with the same total cross-sectional area. The computational domain was segmented into three separate blocks: block 1 is the annular channel (discretized using $42 \times 41$ points in the axial and radial directions respectively), block 2 is the volume over the liquid-delivery-tube (a ring-shaped volume extending radially outward from the liquid-delivery-tube external diameter and bound in the axial direction by the liquid-delivery-tube end; $57 \times 161$ grid points were used), and block 3 is the volume after the axial-end of the liquid-delivery-tube ($289 \times 215$). Blocks 2 and 3 extend radially to a distance of $10R$, while block 3 extends axially to a distance of $14.7R$ from the exit-plane of the annular channel. Based on results for the atomization jet at baseline conditions,[5] the previous grid nodal densities were determined to render grid independent solutions for this type of problem.[4]

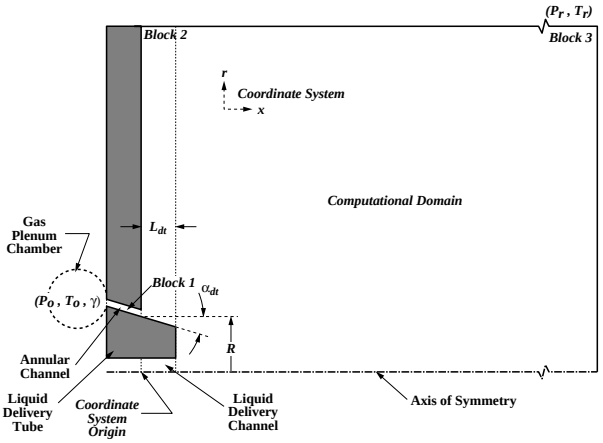


Figure 4. Schematic diagram of the computational domain used to model the gas-only flow in a close-coupled atomizer.

Within each block, the mesh points were distributed using the SAGE grid adaptation program.[14] At all solid boundaries, the first line of points parallel to the wall was forced to be located at $y^+ \simeq 1$ to obtain accurate resolution at the wall layer. As an example, Figure 5 shows one of the final adapted grids used.

Characteristic-type boundary conditions were

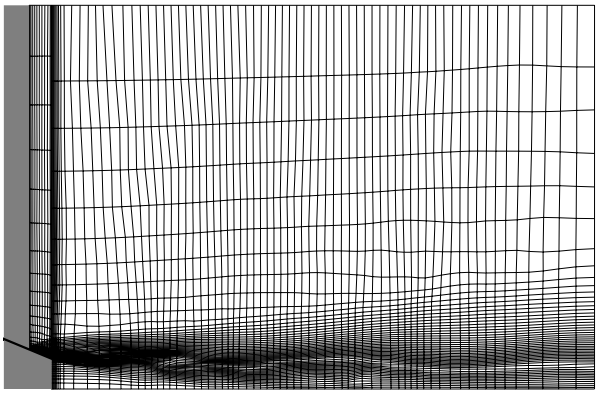

Figure 5. Typical computational mesh adapted for simulation of gas-only flow in a close-coupled gas-metal atomizer (only every fourth grid line is shown for clarity).

used at the inlet of the annular channel ($P_o$, $T_o$ specified) and at the free boundaries of blocks 2 and 3 ($P_r$, $T_r$ specified). The block 1 $\rightleftharpoons$ block 2 interface as well as the block 2 $\rightleftharpoons$ block 3 interface were interpolated explicitly. Axisymmetry was used at the axis of the third block while all other boundaries were treated as adiabatic, non-slip walls.

Additional details regarding the various aspects of the numerical method here used can be found in Refs. 4 and 6.

## Results

Some of the parameters listed in Table 1 are typically fixed by the design of the atomization nozzle assembly: $R$, $r_o/R$ , $\alpha_{jet}$, and $\alpha_{dt}$. Others can be changed prior to the initiation of the atomization process: $L_{dt}/R$, $r_{dt}/R$, and the gas species. However, a number of parameters can be changed *in situ*, providing the ability to modify the atomization process output based on some product quality measurement: $P_r$, $P_e/P_r$, $T_r$, and $T_e/T_r$. In this section, we first perform a critical evaluation of the turbulence model[11,12] by comparing experimental and numerical results for the baseline atomization jet. The remainder of the section is dedicated to the study of pressure- and temperature-ratio effects on the structure of the gas-only atomization flow. Such knowledge can be of assistance in the design of atomizers and in the development of control strategies for them.

### Effects of Turbulence Modeling

Numerical results obtained for a supersonic base flow indicated that the Chien $k$-$\epsilon$ model has difficulty predicting the structure of the recirculation base region – the most important flow area as far as atomization is concern.[4,6] More specificly, the model over-estimates the production of turbulence kinetic energy dissipation rate, $\mathcal{P}_\epsilon$, leading to: 1. an overprediction of the turbulence dissipation rate, $\epsilon$, 2. an underprediction in the turbulence kinetic energy, $k$, and thus, 3. an underprediction of the eddy-viscosity, $\mu_t$. This typically results in an underprediction of the growth rate of the shear layers and a prediction of a delayed reattachment.

In the Chien $k$-$\epsilon$ model, the balance between the production and dissipation of $\epsilon$ is controlled by the magnitude of the $C_{\epsilon 1}$ and $C_{\epsilon 2}$ constants.[12] The value of the $C_{\epsilon 2}$ constant was deduced from the value obtained from the decay of high-Reynolds-number grid turbulence by Hanjalic and Launder.[15] The value of $C_{\epsilon 1}$ was obtained by keeping the difference between $C_{\epsilon 1}$ and $C_{\epsilon 2}$ as prescribed by Jones and Launder;[16] a selection that yields the production and dissipation of $\epsilon$ in near balance for wall bounded flows.

Recently, Yakhot *et al.*[17] made use of renormalization group (RNG) methods to develop explicitly a $k$-$\epsilon$ model that differs from Chien's in the addition of an extra production term to the $\epsilon$ equation. This extra term becomes significant in rapidly distorted flows, and thus, it is likely to have a significant magnitude in supersonic base flows. In their work, Yakhot *et al.*[17] modeled this extra production term as a modification to the turbulent dissipation production constant, $C_{\epsilon 1}$, given as

$$C^*_{\epsilon 1} = C_{\epsilon 1} - \frac{\eta(1-\eta/\eta_0)}{1+\beta\eta^3} \qquad (1)$$

where $\eta = k/\epsilon\sqrt{2S_{ij}S_{ij}}$, $\eta_0$ is a fixed point constant, and $\beta$ is a constant determined from testing the model in well characterized flows (*e.g.,* turbulent boundary layer).

The use of Yakhot's RNG model led to mixed results in the simulation of supersonic base flows.[4] In particular, the RNG $k$-$\epsilon$ model proved to be more destabilizing than the original Chien $k$-$\epsilon$ model, decreasing the local value of $C_{\epsilon 1}$ in some regions (a desirable effect), but increasing the local value of $C_{\epsilon 1}$ above Chien's 1.35 threshold in other regions of the flow (an undesirable effect). The instability problem persisted even when the value of $C_{\epsilon 1}$ was prevented from rising above 1.35 apparently due to the resulting unphysical distribution of $\epsilon$. However, the notion of reducing the production of $\epsilon$ due to the inherent lack of local isotropy in rapidly distorted flows,[18] led Espina[4] to use a globally reduced

value of $C_{\epsilon 1}$ in the standard Chien's $k$-$\epsilon$ model. It was found that a 10% reduction in the production of turbulence dissipation rate yields results that are in good agreement with the experimental findings of Herrin and Dutton[19] for the supersonic base flow case.

To determine the proper level of turbulence dissipation rate production for atomization flows produced by the selected geometry, three values of the model constant, $C_{\epsilon 1}$, were tested: the original Chien's $k$-$\epsilon$ model[12] ($C_{\epsilon 1} = 1.35$), a 10% global reduction in $\mathcal{P}_\epsilon$ ($C_{\epsilon 1} = 1.215$), and a 20% global reduction in $\mathcal{P}_\epsilon$ ($C_{\epsilon 1} = 1.08$). Figure 6 compares the density distributions obtained in these simulations against a Schlieren image of the same flow field.

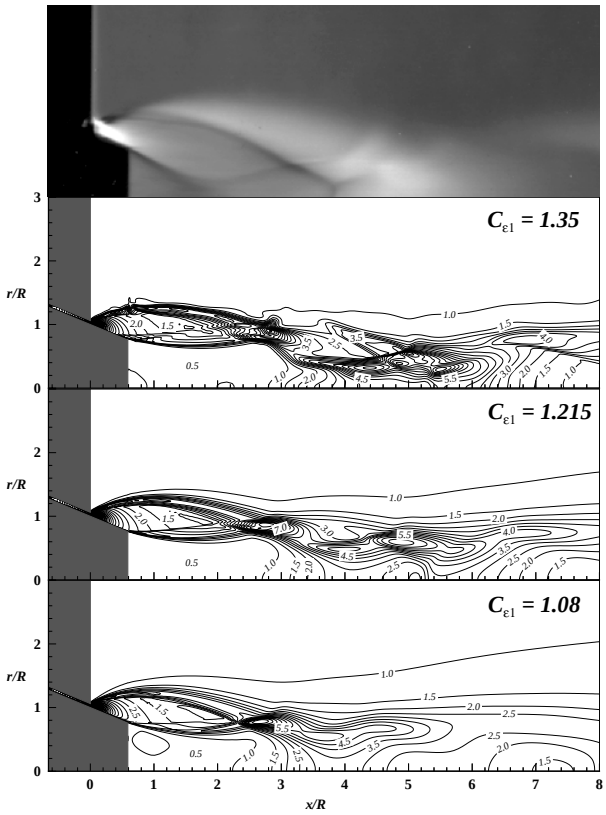


Figure 6. Effect of the turbulence dissipation rate production level on the density distribution of the gas-only atomization flow (baseline settings): experimental Schlieren picture (top image), numerical density distributions, $\rho^* = \rho/\rho_r$ (lower images): $\rho_r = 1.66\ kg/m^3$, $\Delta\rho^* = 0.5$.

The results yielded by the original Chien $k$-$\epsilon$ model (second image from the top in Figure 6) exhibited an instability of the outer shear layer that originated at the end of the annular channel and was amplified as the flow progressed downstream – see irregularities in the $\rho/\rho_r = 1$ contour. This instability, which could be either numerical or due to the inflection point in the mean velocity profile, was not followed accurately in time. Other stable features of the solution appeared to be in disagreement with the experimental data: first, the real atomizer flow (Figure 6, top) exhibits a crossing between the two initial shock waves at $x/R \simeq 3.2$, $r/R \simeq 0.5$; in the numerical result, this crossing occurs at $x, R \simeq 1.8$, $r/R \simeq 1.0$. This produces a shorter than expected first barrel-shock structure[‡] which, in turn, leads to a larger number of barrel-shocks in the length of the jet than there are in the real flow. Second, in the real atomization jet, the inner shear layer projects inward, towards the axis of symmetry, to a maximum radial distance of 0.3; in the numerical result, it only deflects to a distance of 0.6. This leads to differently shaped base flow regions, the real one having an hourglass shape whereas the numerical one looks like a slightly pinched cylinder. Third, the numerical results led to an unphysical supersonic recirculating region (—— in Figure 7, $M_{max} = 1.79$) that extended to $x/R = 4.00$, and in turn, to a positive pressure at the center of the liquid-delivery-tube face (—— in Figure 8) which is in disagreement with the averaged experimental findings (—— in Figure 8).

Figure 6 (third from the top) shows the results obtained with a 10% global reduction in the production of turbulence dissipation rate. At this level of $\mathcal{P}_e$, the results yielded a stable outer shear layer and a crossing between the two initial shock waves at $x/R \simeq 2.1$, $r/R \simeq 0.9$. The inner shear layer projected inward, towards the axis of symmetry, to a maximum radial distance of 0.6. However, the shape of the separation region is in better agreement with the experiment than the one predicted by the original Chien $k$-$\epsilon$ model case. For this 10% reduction case, the numerical results led to a fully subsonic recirculating region (- - - in Figure 7, $M_{max} = 0.99$) that extended to $x/R = 3.69$. This slower separation region produced a base pressure distribution (- - - in Figure 8) in better agreement with the experimental findings (—— in Figure 8) than the original Chien $k$-$\epsilon$ model estimation. However, the high Mach number continued to contribute to a signifi-

[‡] A "barrel-shock" is a repetitive barrel-shaped flow structure initiated by an expansion fan and terminated by an oblique shock wave. The resulting flow pattern is often seen in supersonic jets as a series of diamonds (see Ref. 20).

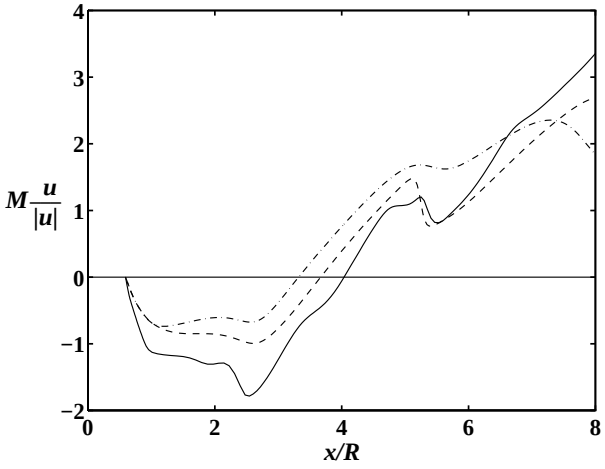


Figure 7. Effect of turbulence dissipation rate production level on axial Mach number distribution of the gas-only atomization flow (baseline settings). ——— : original Chien's $k$-$\epsilon$ model ($C_{\epsilon 1} = 1.35$); – – – : 10% global reduction in $\mathcal{P}_\epsilon$ ($C_{\epsilon 1} = 1.215$); -·-·- : 20% global reduction in $\mathcal{P}_\epsilon$ ($C_{\epsilon 1} = 1.08$).

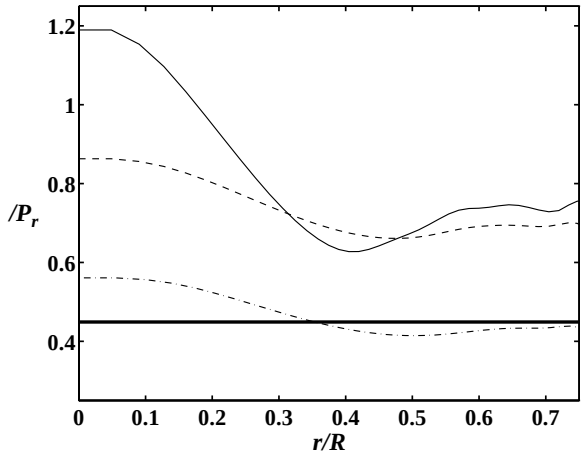


Figure 8. Effect of turbulence dissipation rate production level on base pressure distribution of the gas-only atomization flow (baseline settings). ——— : original Chien's $k$-$\epsilon$ model ($C_{\epsilon 1} = 1.35$); – – – : 10% global reduction in $\mathcal{P}_\epsilon$ ($C_{\epsilon 1} = 1.215$); -·-·- : 20% global reduction in $\mathcal{P}_\epsilon$ ($C_{\epsilon 1} = 1.08$); ——— : experimental data (averaged value only), $P_{r_{exp}} = 98.574\ kPa$.

cant discrepancy in the base pressure between the experiments and the numerical prediction.

Encouraged by the results obtained at 10% reduction levels, we proceeded to simulate the flow with a 20% global reduction in the production of the turbulence dissipation rate. The results obtained at this level (Figure 6, bottom image) yielded the crossing between the two initial shock waves at $x/R \simeq 2.3$, $r/R \simeq 0.8$ and exhibited no stability problems. The inner shear layer projected inward, towards the axis of symmetry, to a maximum radial distance of 0.5, but the shape of the separation region moved away from the hourglass shape seen in the experiment. The recirculating region (-·-·- in Figure 7) had a length of $x/R \simeq 3.31$ with a maximum Mach number of 0.66. The base pressure distribution (-·-·- in Figure 8) is in excellent agreement with the experimental findings (——— in Figure 8). However, this level of production of turbulence dissipation rate leads to excessively high levels of eddy viscosity that further downstream leads to an earlier-than-expected dissipation of the jet. In fact, at this 20% reduction level, the outer shear layer grows too fast ($x/R|_{num} \simeq 8$, $r/R|_{num} \simeq 2$ vs. $x/R|_{exp} \simeq 8$, $r/R|_{exp} \simeq 1.25$) and no shock waves are seen downstream of $x/R \simeq 3$.

Based on all of the previous findings, the results presented hereafter were obtained with a global 10% reduction in the production of turbulence dissipation rate. The flow predictions obtained this way have a number of differences when compared with the real atomization flow. However, it is our belief that these estimates are as good as can be obtained using a $k$-$\epsilon$ turbulence model, and that they predict the trends with accuracy sufficient to allow for the parametric study of the gas-only atomization flows.

**Effects of Jet Pressure Ratio**

In this section we investigate the effects of jet pressure ratio on the structure of the gas-only flow. We chose to model four jets at pressure ratios of $P_e/P_r = 6.6$, 20, 33, and 46. Density contours are compared to Schlieren images in Figure 9. Overall, good agreement can be observed between experimental data and numerical results; the flow structures (shock waves, expansion fans, shear layers) observed in the experiments are also present in the calculations, and their locations are generally correct.

At $P_e/P_r \simeq 6.6$ (top of Figure 9), the annular portion of the jet displays three barrel-shocks before its transformation into a single jet at $x/R \simeq 2.05$. Upon its separation from the surface of the liquid-delivery-tube, the annular flow encapsulates a conically shaped region at the base of the liquid-delivery-tube. This entrapped flow draws momentum from the main flow across the inner shear layer, leading to relatively fast recirculating velocities inside of it ($M_{max} \simeq 0.76$). After its transforma-

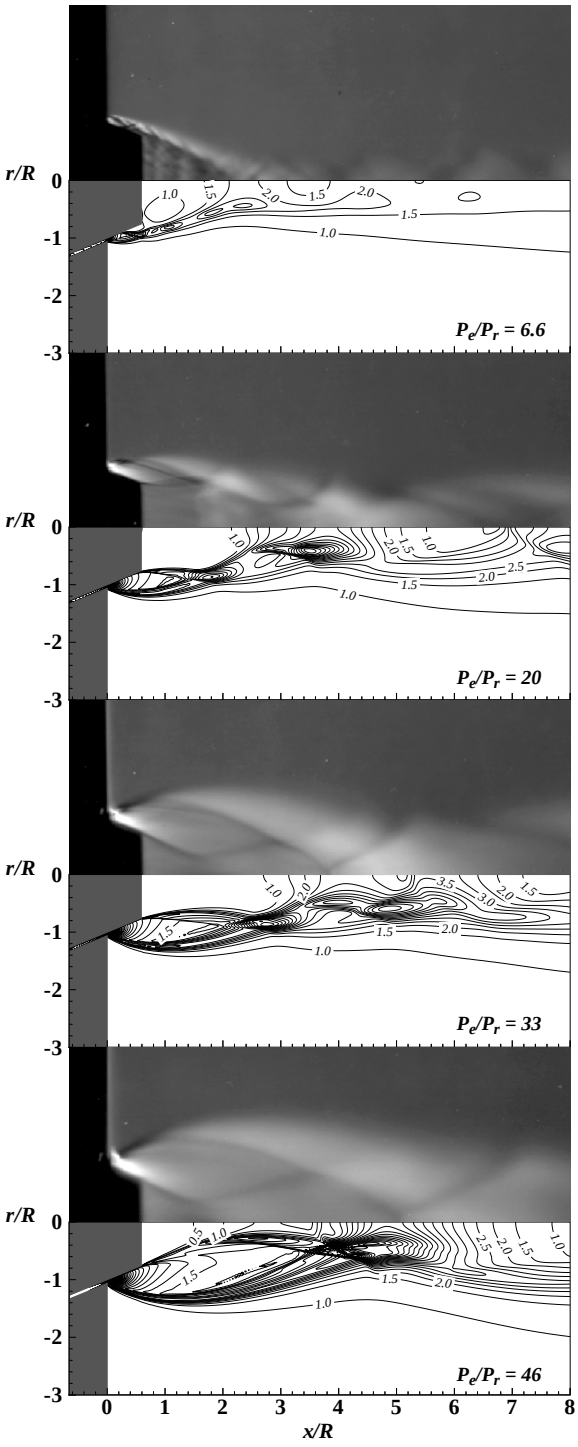


Figure 9. Effects of jet pressure ratio on the structure of gas-only atomization flows (baseline settings except as noted): experimental Schlieren pictures (upper images), numerical density distributions, $\rho^* = \rho/\rho_r$ (lower images): $\Delta\rho^* = 0.5$.

tion into a single jet at $x/R \simeq 2.05$, the gas continues downstream as a supersonic jet up to at least $x/R = 8$, displaying three additional barrel-shocks along that distance. The outer shear layer entrains little surrounding fluid and the jet shows little spreading, attaining a maximum radius of only $1.2\,R$ by $x/R = 8$.

For a pressure ratio of 20 (second image from the top in Figure 9) the annular portion of the flow contains two barrel-shocks: a complete one, followed by the initial portion of a second one. The middle portion of the initial barrel-shock pinches the separation streamline, giving it an hourglass shape. The flow reattaches at $x/R \simeq 2.80$, after the second barrel-shock reaches the axis of symmetry. The outer shear layer draws about twice as much fluid from its surroundings as the $P_e/P_r \simeq 6.6$ jet. This high entrainment, combined with a jet mass flowrate that is three times larger than the mass of the $P_e/P_r \simeq 6.6$ jet, yields a thicker jet with a maximum radius of $1.5\,R$ at $x/R = 8$

The baseline jet, $P_e/P_r \simeq 33$ (third from the top in Figure 9), also shows a complete barrel-shock followed by a partial one in the annular portion of the flow ($x/R < 3.65$). For this pressure ratio, the arrangement of the annular barrel-shocks places the "fat" portion of the initial one (*i.e.,* its middle portion) near the middle of the separation bubble, leading to a longer and narrower separation region than those seen before. At this pressure ratio the annular wave structure persists beyond the reattachment point, changing to a single-jet wave structure at $x/R \simeq 5.2$. When the annular wave structure finally meets the axis of symmetry, it forms a Mach reflection. For this pressure ratio, the flow entrainment is reduced compared to that seen in the $P_e/P_r \simeq 20$ jet. The lower entrainment yields a jet with a maximum radius of $1.7\,R$ (at $x/R = 8$), even though the jet carries 65% more mass than its lower pressure ratio counterpart.

The structure of the high pressure ratio jet, $P_e/P_r \simeq 46$, is different in many ways from the lower pressure ratio cases. At this pressure ratio, the annular flow only contains one barrel-shock with its "fat" portion of it forcing the inner shear-layer very close to the axis of symmetry. This leads to a very short, conically shaped separation bubble ($x/R < 2$) with a small surface area that allows for little momentum flux across the inner shear layer. At this pressure ratio the entrainment increases, drawing as much surrounding fluid as the $P_e/P_r \simeq 20$ jet. The additional entrainment, combined with a 28%

increase in mass flow over the $P_e/P_r \simeq 33$ jet levels, leads to a maximum radius of $2\,R$, at $x/R = 8$. However, at this distance, the jet spreading rate is still under the strong local influence of the wave structures, and the jet radius is a function of the inviscid flow structure as much as it is a function of the flow entrainment.

Figure 10 shows the aspiration pressure as a function of the jet pressure ratio. The experimental results, which are typical of this type of atomizer,[5,21,22] were recorded in the experimental facility used by Espina.[23] At each point, the experimental uncertainty of the data is no larger than the size of the symbols used in the plot.

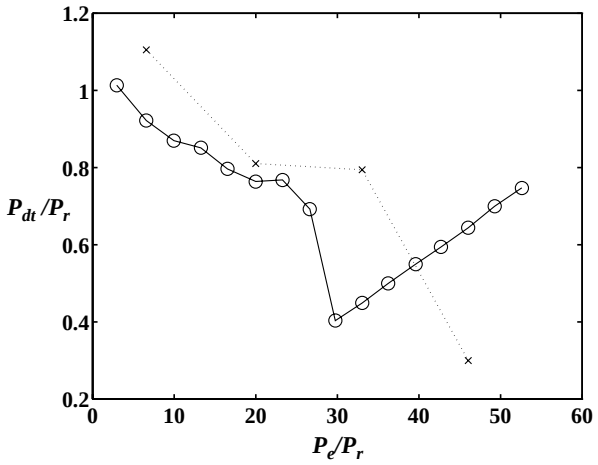


Figure 10. Effect of jet pressure ratio, $P_e/P_r$, on aspiration pressure, $P_{dt}/P_r$, for the selected close-coupled atomization nozzle assembly (baseline settings except as noted). —○— : experimental data, $P_{r_{exp}} = 98.574\ kPa$; —×— : numerical results.

At low pressure ratios, $P_e/P_r < 5$, the liquid-delivery-tube experiences a high aspiration pressure, $P_{dt}/P_r > 1$, that can lead to a "blow-back" condition (*i.e.,* gas flowing into the liquid-delivery-tube and bubbling through the liquid metal in the crucible, generally leading to a freeze-off). For mid-range pressure ratios, $5 < P_e/P_r < 25$, the liquid-delivery-tube records ever decreasing aspiration pressures that plateau near $P_e/P_r \simeq 20$. For a narrow range of pressure ratios thereafter, $25 < P_e/P_r < 30$, the aspiration pressure decreases rapidly, leading to its minimum value, or *maximum aspiration condition.* Further increases in jet pressure ratio lead to linear increases in aspiration pressure, eventually leading to a second blow-back regime.

The numerical calculations generally overpredict the aspiration pressure by 10-20% (a result consistent with similar problems observed in supersonic base flow simulations[4,6]). The initial portion of the curve is predicted better than the region where the transition between decreasing and increasing aspiration pressures occurs. This transition is predicted at higher values of the jet pressure ratio, $P_e/P_r$, by the simulation than observed experimentally.

An important feature of these jets is that flow separation may occur over the outer surface of the liquid-delivery-tube for some conditions (see Figure 11). The occurrence of separation, which is a function of jet pressure ratio and liquid-delivery-tube extension, has been experimentally shown[24] to cause liquid metal to be drawn from the end-face of the liquid-delivery-tube into its outer surface, where it is exposed to the very cold expanding gas of the annular wall jet. The extreme temperature difference between the metal and the gas promotes the solidification and accumulation of metal, leading to a shape alteration of the liquid-delivery-tube. Typically, this sequence of events induces a freeze-off that ends the atomization process prematurely. Therefore, this separation is detrimental to the process of gas-metal atomization and should be avoided at all costs.

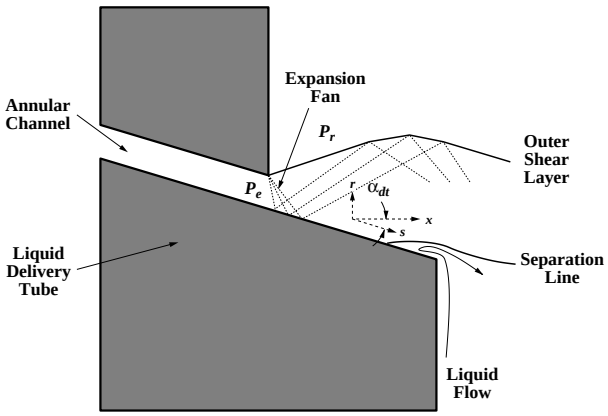


Figure 11. Schematic diagram of the separation phenomenon at the end of the liquid-delivery-tube.

Figure 12 shows the skin friction coefficient, $C_f = 2\,\tau_w/\rho_r a_r^2$, over the surface of the liquid-delivery-tube as a function of surface distance, $s = x/cos(\alpha_{dt})$, for the four pressure ratios. At all pressure ratios, the skin friction coefficient increases early in the length of the liquid-delivery-tube due to the flow acceleration caused by the expansion fan emanating from the end-lip of the annular channel

(see Figure 11). From there on, the skin friction coefficient decays smoothly as the wall jet boundary layer loses momentum to friction.

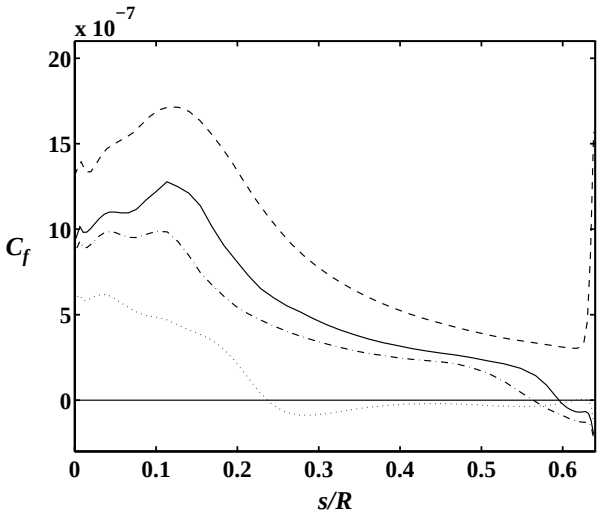


Figure 12. Effect of jet pressure ratio on flow separation over the liquid-delivery-tube (baseline settings except as noted): $C_f = 2\,\tau_w/\rho_r a_r^2$. ·····: $P_e/P_r \simeq 6.6$; -·-·-: $P_e/P_r \simeq 20$; ——: $P_e/P_r \simeq 33$; – – –: $P_e/P_r \simeq 46$.

For a low pressure ratio, $P_e/P_r \simeq 6.6$, the simulation predicts that the flow will separate at $s/R \simeq 0.24$. For intermediate pressure ratios, $P_e/P_r \simeq 20$ and 33, the separation may take place only very near the end of the liquid-delivery-tube, if at all. At the high pressure ratio, $P_e/P_r \simeq 46$, the skin friction coefficient, $C_f$, never becomes negative before the end of the liquid-delivery-tube. Near the end of the liquid-delivery-tube, furthermore, the skin friction coefficient increases rapidly due to the second expansion fan that forms at the end-corner of the liquid-delivery-tube.

The observed behavior leads to the following phenomenological model of the aspiration phenomenon that describes the behavior experimentally, shown in Figure 10. For mid-range pressure ratios, $P_e/P_r < 20$ (decreasing $P_{dt}/P_r$ range), the flow over the liquid-delivery-tube separates early on and the decrease in aspiration pressure with increasing jet pressure ratio is the result of an ever larger expansion level due to the increasing underexpansion of the wall jet. At pressure ratios between 20 and 25 (plateau in $P_{dt}/P_r$ range), the flow separates later, leading to an aspiration pressure level that is controlled by the dynamics of the flow in the hourglass shaped separation bubble. For higher pressure ratios, $P_e/P_r > 25$ (increasing $P_{dt}/P_r$ range), the flow never separates from the face of the liquid-delivery-tube and a second expansion fan forms at its end-corner. This second expansion controls both the shape of the separation region and the aspiration pressure. The higher the pressure ratio goes, the higher the pressure before the second expansion process will be. Given that the turning angle at the end of the liquid-delivery-tube is constant, the second expansion process will yield ever smaller separation regions with ever increasing aspiration pressures.

**Effects of Jet Temperature Ratio**

In some metal-powder production facilities, the gas supply is pre-heated[§] in an attempt to decrease the thermal shock that the ceramic liquid-delivery-tube experiences as a consequence of its contact with the hot liquid metal and the cold gas wall-jet. The practice of gas pre-heating, although expensive and difficult to implement, has also been justified on the basis that it increases the energy available in the gas to disrupt the metal liquid. Thus, it could lead to the formation of finer powders. In this section, we examine the effects of jet stagnation temperature by comparing the baseline atomization-flow calculation (see Table 1) with a similar one in which the gas is at a stagnation temperature twice as high.

Figure 13 compares the density distributions of the unheated, baseline flow ($T_e/T_r = 0.65$) with the heated ($T_e/T_r = 1.31$) atomization flow. As expected, the basic structure of the jet remains unchanged, given that it is controlled by the inviscid portion of the flow, which is only a function of the jet pressure ratio. The density of the heated flow, however, changes in a manner inversely proportional to the change in temperature (*i.e.*, $\rho_{hot}/\rho_{cold} = T_{cold}/T_{hot} = 1/2$); given that the Mach number distribution remains unchanged and that the speed of sound scales with the square root of the stagnation temperature, the speed of the fluid only increase proportionally to the square root of the temperature increase (*i.e.*, $|V|_{hot}/|V|_{cold} = \sqrt{T_{hot}/T_{cold}} = \sqrt{2/1}$). This leads to a net loss of momentum in the flow field of 29% (*i.e.*, $1-\sqrt{2}/2$), probably reducing the ability of the hot flow to disrupt the liquid metal effectively.

The heated jet appears to entrain about 33% more fluid than the unheated jet, even though it carries 29% less mass than its unheated counterpart. The increased entrainment is not sufficient to

[§]Gas stagnation temperatures as high as $700K$ are typical in industrial atomization facilities.

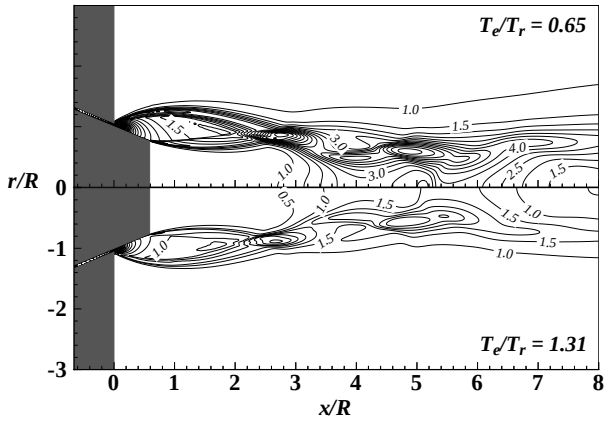


Figure 13. Effects of jet temperature ratio on the density distribution, $\rho^*$, of gas-only atomization flows (baseline settings except as noted): $\Delta\rho^* = 0.5$.

boost the jet spreading rate of the hot flow, whose diameter is 32% smaller by $x/R \simeq 8$ than that of the unheated jet.

The higher stagnation temperature does improve the thermal conditions over the surface of the liquid-delivery-tube. Doubling the stagnation temperature yields an almost constant doubling of the temperature distribution over the liquid-delivery-tube. Given the disparity in temperatures inside and outside of the ceramic liquid-delivery-tube, this wall temperature increase could improve the structural integrity for some ceramic materials with good erosion properties but deficient thermal shock properties (characteristics often encountered among the materials used to manufacture liquid-delivery-tubes).

## Conclusions

The gas-only flow fields produced by a generic close-coupled gas-metal atomizer were computed using methodologies previously tested in similar supersonic base flow configurations.[4,6] Simulations were carried out to determine the effects of jet pressure ratio and gas pre-heating on the gas-only atomization flow.

Four jet pressure ratios were tested, $P_e/P_r = 6.6$, 20, 33, 46. The numerical results showed that, although the aspiration pressure was not predicted with satisfactory accuracy, the resulting jet structure was in good qualitative agreement with experimental Schlieren pictures. The wall jet flowing over the liquid-delivery-tube separated for a certain set of conditions leading to a possible freeze-off condition. Given the severe consequence of flow separation over the liquid-delivery-tube for the atomization process, it is advisable to make use of short liquid-delivery-tubes to avoid flow separation. The separation behavior seen, in conjunction with the observed jet structure, lead to a phenomenological model which describes the aspiration behavior observed experimentally. Our results suggest that the operation of the atomizer in the increasing $P_{dt}/P_r$ range (*i.e.,* $P_e/P_r$ higher than that which yields the minimum aspiration pressure) reduces the chances of separation at the end of the liquid-delivery-tube, thus avoiding the costly possibility of a freeze-off.

The effects of gas heating were studied to determine the effects of this industrial practice on the gas-only atomization flow. Heated jets were shown to have less momentum than their unheated counterparts, which suggests that heating may be detrimental to the formation of fine metal powder. In addition, it was shown that increasing the jet temperature ratio leads to a proportional increase in the gas temperature that may improve conditions to avoid thermal shock of the liquid-delivery-tube material. In our opinion, however, the practice of gas-heating should be avoided unless the need to preserve the structural integrity of the liquid-delivery-tube material absolutely requires it.

## Acknowledgements

This investigation was sponsored by the Chemical Science and Technology Laboratory of the National Institute of Standards and Technology (NIST) under the guidance of Drs. George E. Mattingly and Gregory J. Rosasco. Computational support was provided by the High Performance Systems and Service Division at NIST. In addition, enlightening discussions with Dr. Stephen D. Ridder, and Mr. Francis S. Biancaniello of NIST are gratefully acknowledged.

## References

[1] Lawley, A., "Powder Metallurgy and Rapid Solidification — Compelling Technologies," *J. Metals*, Vol. 37, pp. 15.

[2] Beddow, J. K., *The Production of Metal Powders by Atomization*, Heyden & Son, Ltd., London, 1978, pp. 45.

[3] Boettinger, W. J., Bendersky, L., and Early, J. G., "An Analysis of the Microstructure of Rapidly Solidified Al-8 Wt. Pct. Fe Powder," *Met. Trans. A*, Vol. 17, No. 1, pp. 781–790.

[4] Espina, P. I., "Study of an Underexpanded Annular Wall Jet Past an Axisymmetric Backward-Facing Step," Ph.D. Dissertation, University of Maryland, College Park, MD, Sept. 1997.

[5] Ridder, S. D., and Biancaniello, F. S., "Process Control During High Pressure Atomization," *Mat. Sci. Eng.*, Vol. 98, pp. 47–51.

[6] Espina, P. I., and Piomelli, U., "A Validation of the NPARC Code in Supersonic Base Flows," AIAA Paper 97–0032, Jan. 1997.

[7] Pulliam, T. H., and Steger, J. L., "Implicit Finite-Difference Simulation of Three-Dimensional Compressible Flows," *AIAA J.*, Vol. 18, No. 2, pp. 159–167.

[8] White, F. M., *Viscous Fluid Flow*, 2nd edition, McGraw-Hill, Inc., 1991, pp. 28–32.

[9] Cooper, G. K. and Sirbaugh, J. R., "PARC Code: Theory and Usage," Sverdrup Technology, Inc., Arnold Engineering Development Center, AEDC–TR–89–15, Arnold AFB, TN, Dec. 1989.

[10] Beam, R., and Warming, R. F., "An Implicit Finite Difference Algorithm for Hyperbolic Systems in Conservation Law Form," *J. Comp. Phys.*, Vol. 22, No. 1, pp. 87–110.

[11] Georgiadis, N. J., Chitsomboon, T., and Zhu, J., "Modification of the Two-Equation Turbulence Model on NPARC to a Chien Low Reynolds Number $k$-$\epsilon$ Formulation," NASA TM–106710, 1994.

[12] Chien K.-Y., "Predictions of Channel and Boundary-Layer Flows with a Low-Reynolds-Number Turbulence Model," *AIAA J.*, Vol. 20, No. 1, pp. 33–38.

[13] Sahu, J., and Danberg, J. E., "Navier-Stokes Computations of Transonic Flows with a Two-Equation Turbulence Model," *AIAA J.*, Vol. 24, No. 11, pp. 1744–1751.

[14] Davies, C. B. and Venkatapathy, E., "Application of a Solution Adaptive Grid Scheme to Complex Three-Dimensional Flows," *AIAA J.*, Vol. 30, No. 9, pp. 2227–2233.

[15] Hanjalic, K., and Launder, B. E., "Contribution Towards a Reynolds-Stress Closure for Low-Reynolds-Number Turbulence," *J. Fluid Mech.*, Vol. 74, pp. 593–610.

[16] Jones, W. P., and Launder, B. E., "The Prediction of Laminarization with a 2-Equation Model of Turbulence," *Int. J. of Heat and Mass Transfer*, Vol. 15, pp. 301–314.

[17] Yakhot, V., Orszag, S. A., Thangam, S., Gatski, T. B., and Speziale, C. G. "Development of turbulence models for shear flows by a double expansion technique," *Phys. Fluids A*, Vol. 4, No. 7, pp. 1510–1520.

[18] Durbin, P. A. and Speziale, C. G., "Local Anisotropy in Strained Turbulence at High Reynolds Numbers," *ASME J. Fluids Eng.*, Vol. 113, No. 4, pp. 707–708.

[19] Herrin, J. L., and Dutton, J. C., "Supersonic Base Flow Experiments in the Near Wake of a Cylindrical Afterbody," *AIAA J.*, Vol. 32, No. 1, pp. 77–83.

[20] John, J. E. A., *Gas Dynamics*, 2nd edition, Allyn and Bacon, Inc, Boston, 1984, pp. 161–162.

[21] Ayers, J. D., and Anderson, I. E., "Very Fine Metal Powders," *JOM*, Vol. 37, No. 8, pp. 16–21.

[22] Ting, E. Y., and Grant, N. J., "Metal Powder Production by Gas Atomization," *Progress in Powder Metallurgy*, MPIF, Vol. 41, pp. 67–86.

[23] Espina, P. I., "An Investigation of the Compressible Flow in a Supersonic Inert Gas-Metal Atomizer," Master Thesis, University of Maryland, College Park, MD, 1991.

[24] Ridder, S. D., Osella, S. A., Espina, P. I., and Biancaniello, F. S., "Intelligent Control of Particle Size Distribution During Gas Atomization," *Int. J. of Powder Met.*, Vol. 28, No. 2, pp. 133–138.